

Control-Oriented Modeling of Pipe Flow in Gas Processing Facilities[★]

Sven Brüggemann^a Robert H. Moroto^b Robert R. Bitmead^a

^a*Mechanical & Aerospace Engineering Department, University of California, San Diego, CA 92093-0411, USA, (e-mails: {sbruegge, rbitmead}@eng.ucsd.edu)*

^b*R. H. Moroto was formerly with Solar Turbines Incorporated, San Diego CA 92123, USA (e-mail: rhmoroto@gmail.com).*

Abstract

Pipe flow models are developed with a focus on their eventual use for feedback control design at the process control level, as opposed to the unit level, in gas processing facilities. Accordingly, linearized facility-scale models are generated to describe pressures, mass flows and temperatures based on sets of nonlinear partial differential equations from fluid dynamics and thermodynamics together with constraints associated with their interconnection. As part of the treatment, the divergence of these simplified models from physics is assessed, since robustness to these errors will be an objective for the eventual control system. The approach commences with a thorough analysis of pipe flow models and then proceeds to study their automated interconnection into network models, which subsume the algebraic constraints of bond graph or standard fluid modeling. The models are validated and their errors quantified by referring them to operational data from a commercial gas compressor test facility. For linear time-invariant models, the interconnection method to generate network models is shown to coincide with automation of Mason's Gain Formula. These pipe network models based on engineering data are the first part of the development of general facility process control tools.

1 Introduction

Gas processing facilities, where natural gas is received, treated and compressed for onward transmission through a distribution pipeline network, provide motivation and embodiment for the development of systematic control-oriented modeling tools suited to the design of process control solutions based on plant schematics and layouts. The control of these plants involves the interconnection of a number of elements including pipes, compressors, heat exchangers, valves and valve manifolds, scrubbers and other process units and volumes. The control splits into two distinct aspects: process control for system-wide operational efficiency and accuracy, and safety systems to ensure unit and plant protection. The two control aspects differ in their timescales and in their scope, with the safety system acting across a wide range of operating points (rather than around a single operating point), being both faster, more highly nonlinear, and more localized to specific unit operation, such as avoiding compressor surge. Our focus will be the process control side with an emphasis on unified plant-wide operational effectiveness. The aim of the paper is to develop interconnectable and reconfigurable unit system models, which are amenable to control design, with an objective of bringing multiinput-multioutput (MIMO) control into the picture for gas processing facilities; firstly from engineering design specifications and then augmented by data-based

tuning.

Control-oriented captures the modeling focus on eventual model-based feedback controller design reflecting: plant operational objectives, the presence and capabilities of selected actuators and sensors, and the possible reconfiguration of operations. More precisely, our models are designed to be used for the following conditions.

Plant: Interconnected networks of pipes and processing elements located at one site on the order of tens of meters (rather than kilometers) in extent.

Objective: Bulk pressure regulation and disturbance flow rejection with flow as control input/manipulated variable.

Sensing/actuation: Sampled at or below 1Hz in line with the plant's regulation objective. The focus is on widespread, reliable and accurate pressure sensing in particular, and on actuation using flow control valves. Sensing of flow with orifice plates is there for corroboration more than for control. Temperature sensing is slow and of limited presence in the plant.

Resonant and acoustic modes: While ever-present in compression systems, are at frequencies beyond the sensor and actuator bandwidth in plants of this size.

Models: Should facilitate control design for this regime and be amenable to tuning by control-savvy plant engineers.

[★] This work was supported by Solar Turbines Incorporated.

Although this is quite a specific scenario, it is fairly representative for gas processing facilities.

The models we seek will be linear(ized), time-invariant (LTI) state-space systems, optionally parametrized by nominal operating point, and capable of systematic interconnection of unit models into facility models using computer-based MIMO control design tools. Models with time delay do not fall into this category and are therefore approximated by control-compliant dynamics if necessary. The *quid pro quo* for this utility is that these models are necessarily simplistic and approximate but that, by characterizing their nature, approximations might be addressed in control design. Inevitably, such modeling relies heavily on engineering knowledge of the specific application but admits fairly general applicability.

The subsystem models are based on simplified approximations to constituent equations from fluid dynamics, coupled partial differential equations (PDEs) plus algebraic equations, and are validated against plant data, including the assessment of model errors.

Fluid dynamics and, particularly, computational fluid dynamics, are well-established subjects centered on high-fidelity modeling of flows given design and boundary conditions; typically, they involve nonlinear PDEs and transport phenomena, which are not amenable to finite-dimensional control design but instead are targeted and tested for simulation. Other pragmatic modeling for pipeline distribution systems [3,16,2] yields ordinary differential algebraic equations (DAEs), which again are not well suited to control design. Although, they can be used directly for controller synthesis in some circumstances [10] and, as noted in [3], if the DAE is of index 1. Theorem 4.1 [3] establishes that the DAEs are indeed of index 1 and so it is possible to rewrite the DAE as an ordinary differential equation (ODE) without the algebraic constraints. Effectively, we complete this conversion here.

For fluid or general mechanical systems we take a lead from Benner *et al.* [3] and Williams *et al.* [26] as examples where graph theoretic methods are applied to generate process models from component descriptions, with the latter paper specifically targeted at control design and the former at modeling for simulation. Williams *et al.* [26] is allied in its control objective with our work here and uses energy as the *lingua franca* to map states between subsystems. The edges of their graphs are energy preserving connections with the dynamics occurring at the nodes. By contrast, Benner *et al.* [3] and we model the dynamics in the edges with the nodes applying the interaction constraints. For our target processes of gas processing plants, this latter structure accords better with the primary process control objective of pressure regulation and secondarily with flow estimation. Thermal energy is a byproduct and reflection of the inefficiency of the process. While of interest, temperature is not the central manipulated variable. However, it is noteworthy that the energy formulation of Williams *et al.* [26] for composite aircraft

systems allows conservation laws to be absorbed into the component models, so that the aggregated state-space model can be directly applied for control design. A recent comprehensive survey of modeling and feedback control design for HVAC systems is provided by Goyal *et al.* [12], which cites Rasmussen & Alleyne [21] who concentrate explicitly on control-oriented modeling in these vapor compression systems. However, because their pipes are short and well-insulated, the system structure again focuses on node dynamics rather than edge dynamics of our problem.

For large-scale domain-independent systems, works from Šiljak and colleagues [20,25,24] follow a top-down approach, decomposing large-scale networks into smaller subsystems, and analyze control-relevant notions, such as (structural) stability, reachability and controllability. While their approach is generally applicable to the case of pipe flow, the logical direction differs: instead of decomposing, we *compose* interconnected systems from subsystems in a bottom-up approach under the assumption that structures are fixed (rendering structural stability [25] secondary). Further, the control actuator and, to a lesser extent, sensor locations are few when compared with the number of subsystems or network elements.

Following [3], which deals with isothermal models of gas distribution networks, we commence by studying pipe flow in individual pipes before considering how these are connected into networks yielding automatable aggregation of subsystems. The authors of [3] propose a network DAE with the algebraic part being the conservation of mass flows at the connection points. At this level of detail, this approach bears a strong resemblance to bond graph techniques [4] from which control design is problematic. However, since the resultant network DAE has index 1, the algebraic part can be solved locally to express some of the variables in terms of the others thereby eliminating them. For our models, algebraic equations arise when pipes join but not when they branch. For joints a state variable is removed yielding a new network element subsuming the three joining pipes. These new elements preserve the linearity and other properties while also respecting the conservation laws. Further, we show how these components might be aggregated into network equations to compute the larger state-space system, which we show subsumes Mason's Gain Formula. That is, we are able to preserve the simplicity of the signal flow model of the pipe network as opposed to resorting to bond graphs or DAEs.

The pipe-flow models developed are validated against 1Hz operating data collected at the Solar Turbines Incorporated Gas Compressor Test Facility (GCTF) at Solar Turbines Incorporated in San Diego. This is a well-instrumented site normally used to test compressor performance. We use engineering design values to derive the parametrized models and then experimental data from a number of recorded tests is used to compare the fit of the data and model outputs. The discrepancy between model and data is used to quantify and qualify the model performance. Specifically, we find

that isothermal models, such as those used in [3], are subject to offsets and slow variations due to temperature gradients, which for this plant are measured but need not necessarily be. Accordingly, the control design needs to accommodate this known inaccuracy of the models. Indeed, the existing single-loop PI-controllers already give this clue and indicate that the principal plant objectives are the regulation of pressures and flows.

The design of network-ready models for pipe flow is the first stage of introducing model-based control design into these systems using engineering design information and data sheets. The project objective is to expand this to include other network elements, such as compressors, heat exchangers, vessels and valves [6], and validate their use for MIMO control design [7].

Part 1: Control-Oriented Pipe Models

We start with a deep dive into: modeling of individual pipe segments as nonlinear PDEs and boundary conditions, spatial discretization to nonlinear ODEs with input signals, then linearized ODE models with inputs. These are then compared with experimental/operational data from the GCTF, yielding control-oriented finite-dimensional linear state-space models and an appreciation of their deviation from ideal behavior. We establish that these single pipe models inherently satisfy conservation of mass flow¹. In Part 2, we explore how to move from pipe models to pipe network models.

2 PDE models

We formulate the pipe dynamics as a one-dimensional flow with standing assumptions common in the literature (e.g. [1,2,3,15]). We assume these throughout the paper.

Standing Assumption 1 *For the one-dimensional pipe flow,*

- (i) *the cross-sectional area of each pipe segment is constant;*
- (ii) *average velocities across the cross section suffice for the computation of the mass flow;*
- (iii) *there is no slip at the wall, i.e. the gas velocity at the inner pipe wall is zero;*
- (iv) *friction along the pipe can be approximated by the Darcy-Weisbach equation, see e.g. [22];*
- (v) *the compressibility factor is constant along the pipe;*
- (vi) *capillary, magnetic and electrical forces on the fluid are negligible.*

¹ This central presence of mass conservation in flow models is more fully examined in our companion model-based control design paper [7]. There, conservation is shown to connect to integrators and inherent model structure at $s = 0$, appreciation of which is critical for regulator design.

Item (ii) is a property of high Reynolds number turbulent flow. Under these assumptions, the constituent relations — Continuity, Momentum, Energy, Gas Equation, respectively — that serve as a basis for our model are

$$\frac{\partial \rho}{\partial t} = -\frac{\partial}{\partial x}(\rho v), \quad (1a)$$

$$\frac{\partial}{\partial t}(\rho v) + \frac{\partial}{\partial x}(\rho v^2 + p) = -\frac{\lambda}{2d}\rho v|v| - g\rho\frac{dh}{dx}, \quad (1b)$$

$$\begin{aligned} q\rho = \frac{\partial}{\partial x} \left[\rho v \left(c_v T + \frac{v^2}{2} + gh + \frac{p}{\rho} \right) \right] \\ + \frac{\partial}{\partial t} \left[\rho \left(c_v T + \frac{v^2}{2} + gh \right) \right], \end{aligned} \quad (1c)$$

$$p = \rho R_s T z_0, \quad (1d)$$

which are derived in e.g. [17] and whose parameters are defined in Table 1. The boundary conditions

$$p(0, t), \quad q(L, t), \quad T(0, t),$$

are assumed to be known. Continuity Equation (1a) captures conservation of mass. Momentum Equation (1b) is obtained by a Newtonian approach considering forces acting on a fluid. Total Energy Equation (1c) is the First Law of Thermodynamics in differential form, see e.g. [23]. The Gas Equation (1d) closely describes the behavior of natural gas at the conditions pertaining in the handling facility.

We develop a dynamic model for $p(L, t)$ and $q(0, t)$, and if required also for $T(L, t)$, and a related methodology that allows a systematic interconnection of pipe elements in a network. Towards this goal, in Section 3, from the constituent relations above we derive a nonisothermal, linear, 3D state-space model with the pressure, mass flow and temperature as state elements. Under the condition of a constant temperature, in Section 4 we revisit (1) and introduce a simplified isothermal 2D model. In the next section we validate both models against operating data from the GCTF and compare them to the numerical solution of the PDEs in (1). This analysis suggests using the isothermal model parametrized by spatially varying nominal temperature and managing small offsets and slow drifts with the controller design. Section 7 treats the removal of algebraic constraints stemming from the DAEs and proposes a catalog of common network units in state-space form, including a new pipe joint element. To interconnect these unit models to pipe networks, Section 8 contains a matrix methodology, which we prove subsumes and automates Mason's Gain Formula in the MIMO context. The properties of interconnected components are then illustrated by a numerical experiment in Section 9². We finish this paper with a brief conclusion and directions for future research.

² A compendium of linear state-space models for a variety of elements is provided, with derivations, in [6]. This paper also includes examples and MATLAB code for interconnected networks and establishes the mass conservation property of each model.

Symbol	Meaning	SI-unit
A_c	Cross-sectional area	[m ²]
c	Speed of sound	[$\frac{m}{s}$]
c_v	Specific heat	[$\frac{J}{kgK}$]
d	Pipe inside diameter	[m]
\bar{d}	Pipe outside diameter	[m]
g	Gravity constant	[$\frac{m}{s^2}$]
$h(x)$	Pipe elevation	[m]
k_{rad}	Lumped thermal conductivity pipe	[$\frac{W}{m^2K}$]
L	Pipe length	[m]
$p(x, t)$	Pressure	[$\frac{kg}{s^2m}$]
$\tilde{p}(x, t)$	Pressure deviation from nominal point	[$\frac{kg}{s^2m}$]
$q(x, t)$	Mass flow	[$\frac{kg}{s}$]
$\tilde{q}(x, t)$	Mass flow deviation from nominal point	[$\frac{kg}{s}$]
\mathcal{Q}	Rate of heat flow per unit area	[$\frac{W}{m^2}$]
Re	Reynolds number	[1]
R_s	Specific gas constant	[$\frac{m^2}{s^2K}$]
$T(x, t)$	Temperature	[K]
$\tilde{T}(x, t)$	Temperature deviation from nominal point	[K]
T_0	Nominal temperature	[K]
T_{amb}	Ambient temperature	[K]
$v(x, t)$	Velocity	[$\frac{m}{s}$]
z	Compressibility factor	[1]
z_0	Constant compressibility factor	[1]
ϵ	Roughness of pipe wall	[m]
λ	Friction factor	[1]
$\rho(x, t)$	Density	[$\frac{kg}{m^3}$]

Table 1

Definitions of model variables and SI-units.

3 Non linear and linear nonisothermal 3D ODE models

Towards a nonisothermal 3D model with pressure, mass flow and temperature as state elements, consider constituent relations (1). Notice that “3D” refers to the number of states and not the spatial dimension. For the corresponding total energy equation, (1c), the heat flux, \mathcal{Q} , is assumed to be limited to radial conduction through the pipe, so that similar to [19] and neglecting conduction through the gas,

$$\mathcal{Q} \rho A_c dx = k_{rad} \pi \bar{d} dx (T_{amb} - T). \quad (2)$$

This characterization enables the formulation of PDEs that isolate the time derivatives of the desired state variables.

Proposition 1 *Let $|v| \ll c = \sqrt{z_0 R_s T_0}$. Then, constituent*

equations (1) and the heat flux described in (2) yield

$$\begin{aligned} \frac{\partial p}{\partial t} = & \frac{R_s z_0}{A_c c_v} [k_{rad} \pi \bar{d} (T_{amb} - T) \\ & - \frac{\partial q}{\partial x} T (c_v + R_s z_0) + \frac{\partial p}{\partial x} \frac{R_s z_0 T q}{p} \\ & - \frac{\partial T}{\partial x} q (c_v + R_s z_0) + \frac{\lambda R_s^2 z_0^2 T^2 q^2 |q|}{2 d A_c^2 p^2}] , \end{aligned} \quad (3a)$$

$$\frac{\partial q}{\partial t} = -A_c \frac{\partial p}{\partial x} - \frac{\lambda R_s T z_0}{2 d A_c} \frac{q |q|}{p} - \frac{A_c g}{R_s T z_0} \frac{dh}{dx} p, \quad (3b)$$

$$\begin{aligned} \frac{\partial T}{\partial t} = & \frac{R_s z_0 T}{A_c c_v p} \left[k_{rad} \pi \bar{d} (T_{amb} - T) - \frac{\partial q}{\partial x} T R_s z_0 \right. \\ & + \frac{\partial p}{\partial x} \frac{R_s z_0 T q}{p} - \frac{\partial T}{\partial x} q (c_v + R_s z_0) \\ & \left. + \frac{\lambda R_s^2 z_0^2 T^2 q^2 |q|}{2 d A_c^2 p^2} \right]. \end{aligned} \quad (3c)$$

The proof is provided in the Appendix. Proposition 1 enables us to obtain a linear 3D state-space realization, through spatial discretization and subsequent linearization of these PDEs.

We commence with the spatial discretization using simple differences. Subscripts \cdot_ℓ and \cdot_r connote variables at left (entry) and right (exit) sides of the pipe. Input variables are identified with the pipe PDE boundary conditions, p_ℓ , q_r and T_ℓ , and the state variables with the ODE solution, p_r , q_ℓ and T_r , where,

$$\begin{aligned} p_\ell &= p(0, t), & q_\ell &= q(0, t), & T_\ell &= T(0, t), \\ p_r &= p(L, t), & q_r &= q(L, t), & T_r &= T(L, t). \end{aligned}$$

The subscripts are motivated by the definition of a positive x -direction from left to right, but do not imply any specific flow direction, only that one is not free to prescribe both the pressure and flow at a single point. This yields the nonlinear nonisothermal 3D model:

$$\begin{aligned} \dot{p}_r = & \frac{R_s z_0}{A_c c_v} [k_{rad} \pi \bar{d} (T_{amb} - T_r) \\ & - \frac{q_r - q_\ell}{L} T_r (c_v + R_s z_0) + \frac{p_r - p_\ell}{L} \frac{R_s z_0 T_r q_r}{p_r} \\ & - \frac{T_r - T_\ell}{L} q_r (c_v + R_s z_0) + \frac{\lambda R_s^2 z_0^2 T_r^2 q_r^2 |q_r|}{2 d A_c^2 p_r^2}] \end{aligned} \quad (4a)$$

$$\doteq f_p(p_\ell, p_r, q_\ell, q_r, T_\ell, T_r),$$

$$\begin{aligned} \dot{q}_\ell = & -A_c \frac{p_r - p_\ell}{L} - \frac{\lambda R_s T_\ell z_0}{2 d A_c} \frac{q_\ell |q_\ell|}{p_\ell} - \frac{A_c g}{R_s T_\ell z_0} \frac{dh}{dx} p_\ell \end{aligned} \quad (4b)$$

$$\doteq f_q(p_\ell, p_r, q_\ell, T_\ell),$$

$$\begin{aligned}\dot{T}_r = & \frac{R_s z_0 T_r}{A_c c_v p_r} \left[k_{\text{rad}} \pi \bar{d} (T_{\text{amb}} - T_r) - \frac{q_r - q_\ell}{L} T_r R_s z_0 \right. \\ & + \frac{p_r - p_\ell}{L} \frac{R_s z_0 T_r q_r}{p_r} - \frac{T_r - T_\ell}{L} q_r (c_v + R_s z_0) \\ & \left. + \frac{\lambda R_s^2 z_0^2 T_r^2 q_r^2 |q_r|}{2 d A_c^2 p_r^2} \right] \quad (4c) \\ \dot{=} & f_T(p_\ell, p_r, q_\ell, q_r, T_\ell, T_r),\end{aligned}$$

We propose the discretization from (3) to (4) as it approximates reasonable well the original infinite-dimensional at low frequencies relevant for our control problem, as discussed below.

Linearizing (4) results in the MIMO LTI 3D state-space realization,

$$\dot{x}_t = A x_t + B u_t, \quad (5a)$$

$$y_t = x_t, \quad (5b)$$

where $A = \left. \frac{\partial f}{\partial x} \right|_{ss}$, $B = \left. \frac{\partial f}{\partial u} \right|_{ss}$, with $f \doteq [f_p \ f_q \ f_T]^\top$ and $\left. \frac{\partial(\cdot)}{\partial x} \right|_{ss}$ indicating the Jacobian with respect to x evaluated at steady state (denoted by subscript ss), and B written accordingly. Further, the state and input vectors are given by the following deviations from nominal/steady-state values,

$$x_t = [\tilde{p}_r \ \tilde{q}_\ell \ \tilde{T}_r]^\top, \quad u_t = [\tilde{p}_\ell \ \tilde{q}_r \ \tilde{T}_\ell]^\top,$$

with

$$\begin{aligned}\tilde{p}_\ell &= p_\ell - p_{\ell,ss}, & \tilde{p}_r &= p_r - p_{r,ss} \\ \tilde{q}_\ell &= q_\ell - q_{\ell,ss}, & \tilde{q}_r &= q_r - q_{r,ss} \\ \tilde{T}_\ell &= T_\ell - T_{\ell,ss}, & \tilde{T}_r &= T_r - T_{r,ss}.\end{aligned}$$

We stress that for such a state-space realization, which is the basis for modern model-based control design, the preponderance of existing tools in linear systems theory is directly applicable, such as the determination of stability, DC gains, observability and controllability. To assess sufficiency for control-oriented design, we will use this nonisothermal 3D model as a benchmark for the reduced isothermal 2D model introduced next. Where appropriate, we also compare the solution of the linear system to both the nonlinear 3D model, (4), and the original PDEs, (3).

4 Isothermal 2D linear ODE model

Assume that the temperature is constant, i.e. $T(x, t) = T_0$ for all $x \in [0, L]$ and $t \geq 0$. The Continuity, Momentum and Gas Equations in (1) suffice to obtain

$$\frac{\partial p}{\partial t} = -\frac{R_s T_0 z_0}{A_c} \frac{\partial q}{\partial x}, \quad (6a)$$

$$\frac{\partial q}{\partial t} = -A_c \frac{\partial p}{\partial x} - \frac{\lambda R_s T_0 z_0}{2 d A_c} \frac{q |q|}{p} - \frac{A_c g}{R_s T_0 z_0} \frac{dh}{dx} p, \quad (6b)$$

where for the mass flow, q , we additionally used the relation $q = \rho A_c v$. We also neglect the partial derivative of the inertia (or kinematic) term, ρv^2 , justified by the fact that the speed of sound, c , usually greatly exceeds the velocity of the fluid [3, pp. 174]. This is also consistent with Proposition 1.

Following [3], a spatial discretization of (6) yields

$$\dot{p}_r = -\frac{R_s T_0 z_0}{A_c L} (q_r - q_\ell), \quad (7a)$$

$$\dot{q}_\ell = -\frac{A_c}{L} (p_r - p_\ell) - \frac{\lambda R_s T_0 z_0}{2 d A_c} \frac{q_\ell |q_\ell|}{p_\ell} - \frac{A_c g}{R_s T_0 z_0} \frac{h}{L} p_\ell. \quad (7b)$$

Linearizing around nominal points denoted by subscript ss and using tildes to denote perturbation variables, we obtain

$$\dot{\tilde{p}}_r = \alpha (\tilde{q}_r - \tilde{q}_\ell) \quad (8a)$$

$$\dot{\tilde{q}}_\ell = \beta \tilde{p}_r + \kappa \tilde{p}_\ell + \gamma \tilde{q}_\ell, \quad (8b)$$

with

$$\begin{aligned}\alpha &= -\frac{R_s T_0 z_0}{A_c L}, & \beta &= -\frac{A_c}{L}, \\ \kappa &= \frac{A_c}{L} + \frac{\lambda R_s T_0 z_0}{2 d A_c} \frac{q_{ss} |q_{ss}|}{p_{\ell,ss}^2} - \frac{A_c g h}{R_s T_0 z_0 L}, \\ \gamma &= -\frac{\lambda R_s T_0 z_0}{d A_c} \frac{|q_{ss}|}{p_{\ell,ss}}.\end{aligned}$$

The LTI ODEs (8) represent a system that can be equivalently realized by

$$\dot{x}_t = \begin{bmatrix} 0 & -\alpha \\ \beta & \gamma \end{bmatrix} x_t + \begin{bmatrix} 0 & \alpha \\ \kappa & 0 \end{bmatrix} u_t, \quad (9a)$$

$$y_t = x_t \quad (9b)$$

with $x_t = [\tilde{p}_r \ \tilde{q}_\ell]^\top$ as the state vector and $u_t = [\tilde{p}_\ell \ \tilde{q}_r]^\top$ as the input vector.

We note immediately several properties revealed by the linear model. The elements (α, β, γ) of the system matrix are all negative and the matrix possesses two eigenvalues at $\frac{\gamma}{2} \pm \sqrt{\frac{\gamma^2}{4} - \alpha\beta}$. The quantity $\alpha\beta = R_s z_0 T_0 / L^2$ is the square of the resonant frequency of a pipe of length L , since $c = \sqrt{z_0 R_s T_0}$ is the speed of sound. The friction term γ is comparatively small. So the linearized state-space model is that of a lightly damped resonant system.

In addition to stability, the control-oriented nature of the model allows us to deduce important properties, such as controllability. Input matrix B is full row rank, so (A, B) is reachable. If pressure p_r is measured then the system is also observable. Pressure is the simplest and most reliably measured process variable.

The DC gain from u_t to x_t can be readily extracted,

$$G_{DC} = -A^{-1}B = -\frac{1}{\alpha\beta} \begin{bmatrix} \alpha\kappa & \alpha\gamma \\ 0 & -\alpha\beta \end{bmatrix} = \begin{bmatrix} -\frac{\kappa}{\beta} & -\frac{\gamma}{\beta} \\ 0 & 1 \end{bmatrix},$$

and reveals the following. In steady state:

- \tilde{p}_r is equal to \tilde{p}_ℓ with appropriately signed corrections due to non-zero flow and elevation;
- regardless of the pressure, \tilde{q}_ℓ is equal to \tilde{q}_r in steady state, as demanded by conservation of mass;

A more detailed analysis will be provided for the 3D state model in Section 9.

Spatial discretization

The spatial discretization of the PDEs using p_ℓ and q_r as the input signals is neither capricious nor refractory but reflects two central matters: the boundary conditions required to specify the solution for pipe flow and the requirement for reachability of the resultant state-space model. The two are not disjoint. Assuming horizontal pipes, the two PDEs (6a)-(6b) may be combined to yield the damped wave equation.

$$\frac{\partial^2 X}{\partial x^2} - \frac{\lambda c^2}{2dA_c^2} \frac{q|q|}{p^2} \frac{\partial X}{\partial x} = \frac{1}{c^2} \frac{\partial^2 X}{\partial t^2} + \frac{\lambda}{dA_c} \frac{q}{p} \frac{\partial X}{\partial t},$$

for either $X(t, x) = p(t, x)$ or $q(t, x)$ with distinct boundary conditions. This PDE is hyperbolic and requires Dirichlet, Neumann or mixed boundary conditions at both ends to define the solutions [11]. Pressure $p_\ell(t)$ provides the left Dirichlet boundary condition and, via (6b), $q_r(t)$ provides the right mixed boundary condition.

An alternative view of this spatial discretization is that, drawing on the electrical transmission line analogue of the pipe, the voltage/pressure and current/flow at one end of the line/pipe may not be independently prescribed, since they are constrained by the driving-point impedance. From the control system perspective of this paper, the selection of p_ℓ and q_ℓ as input signals would not yield the requisite system model reachability mentioned above.

Cascaded pipe models

As discussed in the introduction, it is our primary concern to provide sufficiently accurate models for frequencies below one Hertz well-suited for process control for facilities with pipes of length of around tens of meters (rather than kilometers). Towards this goal, in Figure 1 below we compare the frequency response of the a single pipe of 30m with those of two 15m pipes and three 10m pipes using the composite model for pipes in series from Section 7.3, which in fact represents a finer discretization. We observe that the behaviors for relevant low frequencies indeed coincide; changes for

high frequencies are outside the relevant range and account for acoustical modes associated with the configurations and boundaries. Per the control objective, the bulk flow modes are preserved while the resonances fall outside the sensor and actuator bandwidths.

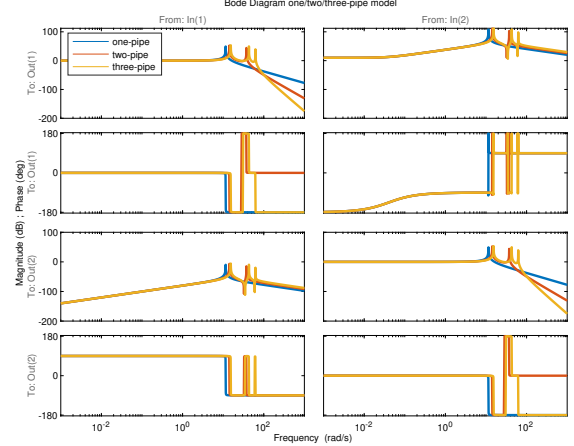


Fig. 1. Comparison of the frequency responses from $\{\tilde{p}_{0,\ell}, \tilde{q}_{n-1,r}\} \rightarrow \{\tilde{p}_{n-1,r}, \tilde{q}_{0,\ell}\}$ with $n = \{1, 2, 3\}$ between one pipe ($n = 1$), two pipes ($n = 2$) and three pipes ($n = 3$) in series with overall identical length.

4.1 Nonisothermal modeling and Bernoulli

To ensure sufficient accuracy of linear models it is important around which nominal point they are applied. Although one may use (7) to generate the corresponding values, we do so by solving the constituent equations in (1) directly for steady-state values. In this fashion, firstly, we are able to accommodate spatially varying temperatures and secondly, we reveal the error inherent to the isothermal assumption and avoid its propagation.

Proposition 2 Suppose at steady state the change in density along the pipe is negligible. Then, the constituent equations in (1) yield

$$q_{r,ss} = q_{\ell,ss}, \quad (10a)$$

$$p_{r,ss} = p_{\ell,ss}^{T_{\ell,ss}/T_{r,ss}} \exp \left(\frac{\lambda L z_0 R_s T_{r,ss}}{2dA_c^2 p_{r,ss}^2} q_{r,ss} |q_{r,ss}| - \frac{gh}{R_s z_0 T_{r,ss}} \right). \quad (10b)$$

If further $|v|, |h| \ll c$, $d \geq \frac{\lambda}{2}$, and $L|v| \ll c$, then

$$p_{r,ss} \approx p_{\ell,ss}^{T_{\ell,ss}/T_{r,ss}} \left(1 - \frac{\lambda L z_0 R_s T_{r,ss}}{2dA_c^2 p_{r,ss}^2} q_{r,ss} |q_{r,ss}| - \frac{gh}{R_s z_0 T_{r,ss}} \right), \quad (10c)$$

where $T_{\ell,ss} = T(0)$ and $T_{r,ss} = T(L)$ at steady state.

PROOF. For brevity, we drop subscript ss in this proof. The nominal mass flow in (10a) follows directly from the continuity equation (1a) by setting the time derivative to zero.

For the nominal pressure in (1b), for the left-hand side, Lurie shows in [17] that

$$\frac{\partial}{\partial t}(\rho v) + \frac{\partial}{\partial x}(\rho v^2) = \rho \left(\frac{\partial v}{\partial t} + v \frac{\partial v}{\partial x} \right).$$

Now assume we are at steady state, so that for $\frac{\partial v}{\partial t} = 0$ and (1b),

$$\begin{aligned} v \frac{\partial v}{\partial x} dx &= -\frac{1}{\rho} \frac{\partial p}{\partial x} dx - \frac{\lambda}{2d} v |v| dx - g dh, \\ \frac{1}{g} v dv &= -\frac{1}{g\rho} dp - \frac{\lambda}{2dg} v |v| dx - dh, \end{aligned} \quad (11)$$

with length dx . We used the fact that the change in velocity, dv , and pressure, dp , along a control volume at steady state is exactly $\frac{\partial(\cdot)}{\partial x} dx$. Without loss of generality we now assume that the height at $x = 0$ is zero. Additionally, under the hypothesis and (10a), we can treat the velocity as a constant so that integrating (11) along the pipe using (1d) yields

$$\frac{v_r^2 - v_\ell^2}{2g} = -\frac{R_s z_0}{g} (T_r \ln p_r - T_\ell \ln p_\ell) - \frac{\lambda L}{2dg} v |v| - h. \quad (12)$$

As $v_r = v_\ell$ and towards an expression for p_r ,

$$\begin{aligned} 0 &= -\ln \left(\frac{p_r^{T_r}}{p_\ell^{T_\ell}} \right) - \frac{\lambda L}{2dR_s z_0} v_r |v_r| - \frac{gh}{R_s z_0}, \\ p_r &= p_\ell^{T_\ell/T_r} \exp \left(-\frac{\lambda L}{2dR_s z_0 T_r} v_r |v_r| - \frac{gh}{R_s z_0 T_r} \right), \end{aligned}$$

which with (1d) gives (10b). By the additional hypothesis,

$$\begin{aligned} |hg| &\ll c^2 = R_s T_r z_0, \\ \lambda \frac{L}{2d} v_r^2 &\leq L v_r^2 \ll c^2 = R_s T_r z_0, \end{aligned}$$

so that

$$\begin{aligned} p_r &\approx p_\ell^{T_\ell/T_r} \left(1 - \frac{\lambda L}{2dR_s z_0 T_r} v_r |v_r| - \frac{gh}{R_s z_0 T_r} \right) \\ &= p_\ell^{T_\ell/T_r} \left(1 - \frac{\lambda L z_0 R_s T_r}{2dA_c^2 p_r^2} q_r |q_r| - \frac{gh}{R_s z_0 T_r} \right), \end{aligned}$$

using again the Gas Equation, (1d).

On the assumptions

For better understanding of conditions under which the assumptions hold and to underline the model's suitability for control, consider Methane with $R_s = 518.28 \frac{\text{J}}{\text{°K mol}}$, a low temperature of $\tilde{T}_r = 300^\circ\text{K}$ and a constant compressibility factor $z_0 = 0.95$. The related speed of sound within the medium is $c = 14.77 \times 10^4 \frac{\text{m}}{\text{s}}$. Hence, the assumptions on the gas velocity, v , height, h , and length, L , conform to typical values in our control domain of gas processing facilities. Also, given a usual friction factor $\lambda \ll 1$, the lower bound on the diameter, d , renders our formula applicable to many industrial scenarios.

Relation to Bernoulli's Equation and isothermal model

The proof of Proposition 2 is of interest in itself since it delineates the relation between the dynamic Momentum Equation, (1b), and static Bernoulli's Equation, (12), commonly used for computing static variables, including a term for head loss, $H_L \doteq \frac{\lambda L}{2dg} v |v|$, often referred to as the Darcy-Weissbach Equation [22]. Furthermore, observe that the approximated nominal point, (10c), coincides with the nominal point derived by the discretized model, (7), under the isothermal assumption and negligible change in density. In other words, Proposition 2 also quantifies the error induced through the isothermal assumption.

5 Model validation

We now wish to assess both the isothermal and nonisothermal models in light of their suitability for control-oriented design, using operational industrial process data from the GCTF. The data fits the problem formulation: it is sampled at 1Hz and describes pressure, mass flow and temperature variations for pipes on the order of tens of meters. Accordingly, it is appropriate for model validation and tuning for this application. Our conclusion is that, for pipe component modeling, the isothermal 2D model is sufficient for model-based control because: temperature variations in these elements are modest, temperature sensing devices can be both limited in number and variable in dynamic response, and variations with temperature can be accommodated by an appropriate controller since they are slowly varying and cause quantifiable gain fluctuations.

Figure 2 shows the facility at Solar Turbines Incorporated. This is a well-instrumented site used for compressor testing and from which comprehensive data sets are available. The particular pipe section under consideration is sketched in Figure 3. Notice that we simplify the stepped pipe geometry by neglecting the stub at the end of the vertical middle section, assuming instead a constant slope and an accordingly adjusted friction factor³. The relevant data is plotted in Fig-

³ We use Haaland's formula [13] to estimate the friction factor for the straight pipes and empirical formulas in [22, Ch. 15] to approximate the friction losses induced by the bends and stub.

ure 4, with behavior in the relevant time scale for our goal of relatively slow process control. We observe that the output pressure, \tilde{p}_r , closely follows the input pressure, \tilde{p}_ℓ , and is higher despite head losses through friction. This is due to the vertical middle section and heat flux causing changes in temperature. As Figure 4 shows, the temperature is relatively constant, but varies with changes in pressure and mass flow. We notice that \tilde{T}_ℓ is measured by a more accurate sensor, given its lower quantization error, which can be observed in the middle zoom. We additionally note that \tilde{T}_r is lower than \tilde{T}_ℓ for most of the time, as is also apparent in the zoom on the right, and it seems to be dynamically faster than \tilde{T}_ℓ , as shown in the left zoom, which may partly be caused by different thermal inertias and processing of the sensors. Given the speed, accuracy and prevalence of pressure sensors, it is apparent that they will provide the primary signals used for feedback control and the quality of capturing the pressure state behavior should be the main model objective. We shall return to this shortly in Subsection 5.3.

5.1 Linear nonisothermal 3D model

We begin by validating the nonisothermal 3D model from Section 4 linearized around the nonisothermal nominal point developed in Proposition 2. In particular, let $q_{r,ss} = \text{mean}(q_r(t))$, $p_{\ell,ss} = \text{mean}(p_\ell(t))$, $T_{\ell,ss} = \text{mean}(T_\ell(t))$ and $T_{r,ss} = \text{mean}(T_r(t))$ so that Proposition 2 yields the corresponding nominal values $p_{r,ss}$ and $q_{\ell,ss}$. We then use \tilde{p}_ℓ and \tilde{q}_r from the data set as model inputs and compare our modeled pressure \tilde{p}_r against the related pressure in the data, recalling that data of \tilde{q}_ℓ for comparison with our model output is not available. Additionally, we study the linear model against the PDEs in (1) solved numerically as a two-point boundary value problem, and to which we refer as the *PDE model*. The lumped thermal conductivity, k_{rad} , is approximated at quasi steady state following [19, Section 3], using $T_{\ell,ss}$ and $T_{r,ss}$. The simulation results are shown in Figure 5.

For the nonisothermal 3D linear model, we see that the simulated output \tilde{p}_r is in a small neighborhood of the measured pressure, but has a small offset. Additionally, we observe that the modeled mass flow \tilde{q}_ℓ is close to the data input, \tilde{q}_r . This is expected for the short length of the pipe $L \approx 30\text{m}$ and sampling rate of once per second. The zoom reveals that when the pressure increases at around 800s, the model output \tilde{q}_ℓ first increases before the signal input \tilde{q}_r follows suit.



Fig. 2. Gas compressor test facility (GCTF) at Solar Turbines Incorporated. [9]

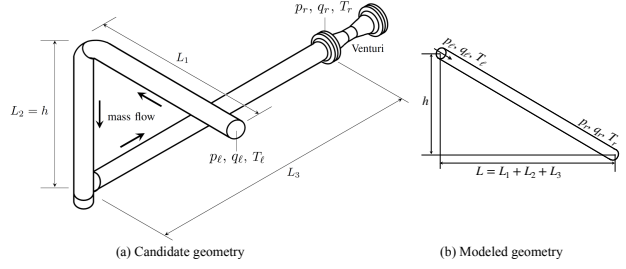


Fig. 3. GCTF pipe section considered for model validation.

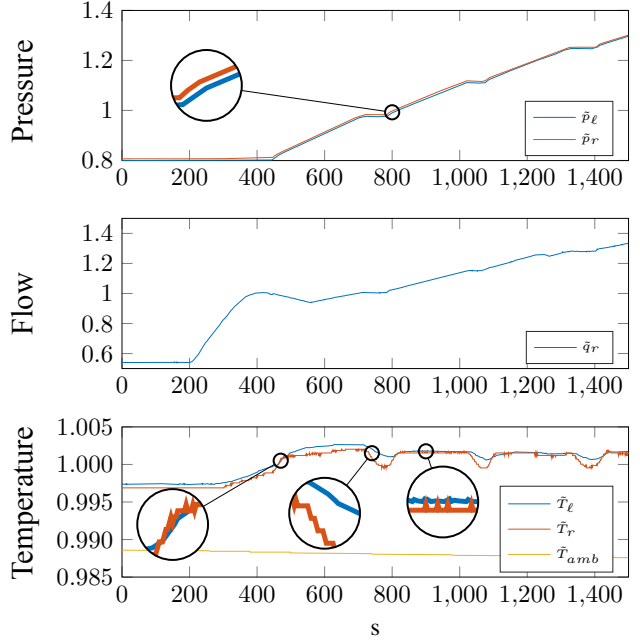


Fig. 4. Normalized data from GCTF. The variables \tilde{p}_ℓ , \tilde{q}_r and \tilde{T}_ℓ will be used as model inputs, whereas \tilde{p}_r and \tilde{T}_r will be used to validate the corresponding model outputs. We observe quantization errors and measurement noise.

This is consistent with a positive mass flow that increases first at the gas entry side of the pipe.

The temperature calculations from the successive models, while close (within 0.64K), exhibit more variability than those of pressure and mass flow. The computed \tilde{T}_r values also exceed the \tilde{T}_ℓ data at times, especially for the linear model. Further, there are times, around 500s for example, where the \tilde{T}_r data also exceeds \tilde{T}_ℓ data. These discrepancies indicate two types of problem: the entry and exit temperature sensors have differing response times and accuracies, as is common in application; and the heat flux model in (2) is too simplistic to capture the dependence of heat flux on velocity and geometry. (See [14] for more detailed analysis of these phenomena.) From a control-oriented perspective, this adds further weight to accommodating these slow variations –

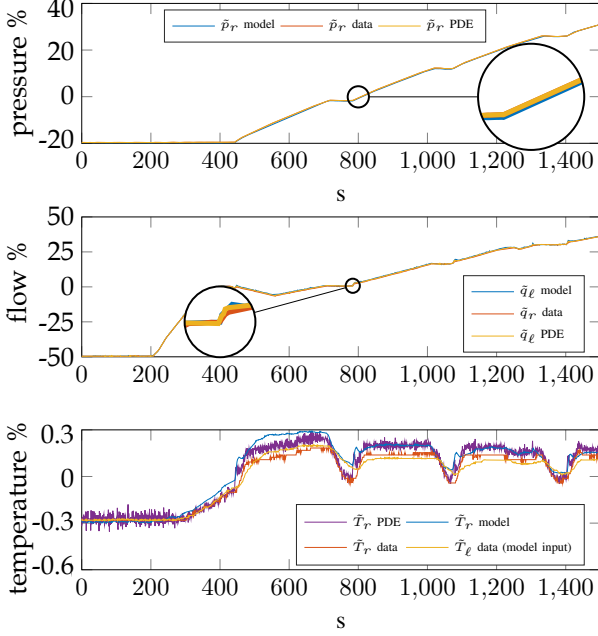


Fig. 5. Percentage deviations from the nominal point (determined as shown above) of the nonisothermal 3D linear model with data as model inputs, compared against GCTF data and PDE model (1).

we quantify time constants shortly in Subsection 5.3 via eigenvalue analysis – through the design of the controller and to preserve the parsimony of the linear model, which captures the salient dynamics.

5.2 Linear isothermal 2D model

Consider now the isothermal 2D model for which the model parameters and nominal point are equal to those of the nonisothermal 3D model above, except the temperature, which we set to $T_0 = (T_{\ell,ss} + T_{r,ss})/2$. As before, \tilde{p}_ℓ and \tilde{q}_r from the data set are model inputs, and we compare the modeled pressure \tilde{p}_r against \tilde{p}_r from the data. The result is shown in Figure 6. Notice that the modeled responses for pressure and mass flow seem congruent with those of the nonisothermal 3D model, i.e., the modeled pressure is close to the measured pressure, but displays a small static offset. The mass flows at both ends of the pipe are close, consistent with conservation of mass at steady state.

5.3 Isothermal 2D vs. nonisothermal 3D model

The results above are now evaluated in view of the control-oriented aspect of our approach. The similarity of both the isothermal and nonisothermal model and their accuracy characterize Figure 7, which shows the relative error between the modeled and measured pressure. The errors of the respective models are closely aligned, rather constant and at most at a rate of 4×10^{-3} . Both the isothermal 2D and the nonisothermal 3D linear models exhibit almost identical small offsets in simulated pressure and both capture the pressure dynamics accurately. From a control design perspective, the

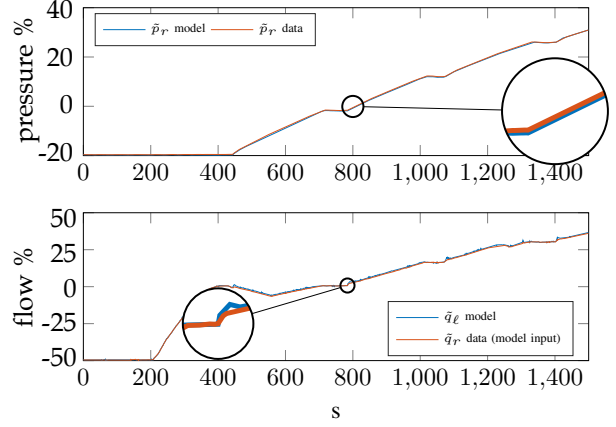


Fig. 6. Isothermal 2D model with percentage deviations from the nominal point, compared against GCTF data and driven by the respective data inputs.

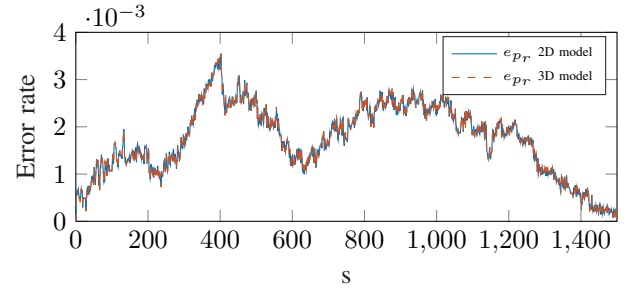


Fig. 7. Respective p_r pressure percentage errors of the isothermal 2D and nonisothermal 3D models.

controller can be constructed to accommodate this modeling error.

Computing the eigenvalues of the system matrices of the related isothermal 2D and nonisothermal 3D linear models, respectively A_{iso} and A_{niso} , and of the truncation of A_{niso} to its first two rows and columns, $[A_{niso}]_{1:2}$, we have

$$\begin{aligned} \text{eig}(A_{iso}) &= (-3.90 \pm 12.47i), \\ \text{eig}(A_{niso}) &= (-3.90 \pm 14.31i, -0.12), \\ \text{eig}([A_{niso}]_{1:2}) &= (-3.88 \pm 14.31i) \\ &\approx \text{eig}(A_{iso}). \end{aligned}$$

From this, we conclude that the temperature state is both effectively decoupled from the pressure and mass flow states and, further, governed by a time constant approximately thirty times that of the reduced-order 2D system, which preserves the dominant lightly damped oscillatory dynamics. Consequently, for moderate temperature gradients, it is reasonable to take the temperature as a constant and employ the isothermal 2D model.

Pressing on with this control-oriented analysis, we note the

respective DC gains,

$$\lim_{t \rightarrow \infty} x_t^{2D} = -A_{iso}^{-1} B_{iso} = \begin{bmatrix} 1.004 & -600.19 \\ 0 & 1 \end{bmatrix},$$

$$\lim_{t \rightarrow \infty} x_t^{3D} = -A_{niso}^{-1} B_{niso} = \begin{bmatrix} 1.004 & -600.33 & -25.35 \\ 0 & 1 & 0 \\ 0 & 0.03 & 0.92 \end{bmatrix}.$$

Continuing the discussion in Section 4, steady-state conservation of mass flow follows for both models as the DC gains from $(\tilde{p}_\ell, \tilde{T}_\ell) \rightarrow \tilde{q}_\ell$ are zero and $\tilde{q}_r \rightarrow \tilde{q}_\ell$ is precisely one. For the steady-state pressure, there is (to two decimal places) a unity gain from $\tilde{p}_\ell \rightarrow \tilde{p}_r$, indicating that changes due to friction and height differences are marginal (cf. κ in Section 4), and a drop of similar size for both models from $\tilde{q}_r \rightarrow \tilde{p}_r$ due to additional friction (cf. γ in Section 4) for this example. The negative gain from $\tilde{T}_\ell \rightarrow \tilde{p}_r$ for the nonisothermal model may be due to larger heat losses to the environment; a characteristic not captured by the isothermal model. Yet, given the magnitude of the SI units used here and low temperature variations in pipe elements, the consequential discrepancy is small, as corroborated by the simulations.

The isothermal 2D model, which relies only on mass flow and pressure measurements, dovetails with the fact that especially pressure sensors (in contrast to temperature sensors) are usually well-distributed in gas processing facilities, fast and reliable. The 2D isothermal model will be used for pipe segments and the control design will be expected to accommodate the small offsets and slow variation of dynamics with changing temperatures. The experimental results and customary practice of sparse temperature measurements (also due to slow temperature sensing responses) suggest that temperatures in typical pipes need not directly be modeled using the 3D model; exceptions are heat exchangers, compressors and other strongly temperature-affecting devices. Driven by this evaluation, we continue the exposition with a focus on this isothermal model.

Part 2: Control-Oriented Models of Pipe Networks

6 DAEs, Signal Flow Graphs and Bond Graphs

Bond graphs [4] provide a systematic method for deriving dynamic equations for interconnected electro-mechanical-hydraulic systems. They combine *effort* variables and *flow* variables, with component properties linking the two types and conservation laws and continuity governing the flows at interconnection. In the framework of fluid flow in pipe networks [17,3], this leads to a set of PDEs for the dynamics combined with algebraic equations for the constraints. Discretizing the spatial derivative yields DAE system models, which are problematic for direct control design for these interconnected systems. By contrast, Signal Flow Graphs (SFGs) correspond to systems described exclusively by

ODEs; transfer functions in the linear case. Interconnected systems are directly managed by methods such as Mason's Gain Formula for the linear case, or by writing the composite state variable ODEs without algebraic constraints. It is these latter model forms, which are amenable to control design tools.

We consider three fundamental interconnections of pipe elements: series connection, branching and joining. Using the isothermal 2D model above, we develop a catalog of composite models that describe common units in the form of interconnections of pipes. In this way, algebraic constraints and DAEs will be avoided, as exemplified through the component of joining pipes introduced first. For clarity, (1) we limit this section to the 2D model, but the methodology is equivalently applicable to the 3D model; and (2) without loss of generality, we assume that the steady state mass flow, q_{ss} , is positive. That is, \cdot_ℓ denotes the side where the steady state mass flow enters the pipe and \cdot_r the side with an outgoing mass flow; hence the denomination *joint* and *branch* to come.

The reduced state vector demonstrates that an interconnection of single pipes into more complex components, with corresponding algebraic constraints, cannot immediately be translated to a SFG using only single pipe models. We also point out that on the contrary, bond graphs [4] are able to represent more complex components including algebraic constraints. However, constraints, such as those in (13), would lead to a causal conflict of type 1 and degree 1 [4, Definition 4.19], which in turn implies the existence of DAEs and therefore disaccords with our objective of control-oriented modeling.

7 From DAEs of index 1 to composite models

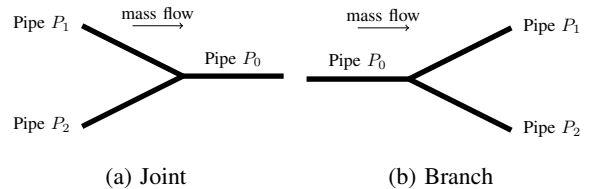


Fig. 8. Pipe junctions

7.1 Joint

Consider the joint shown in Figure 8(a) and let $p_{i,\ell}$ ($p_{i,r}$) be the pressure p_ℓ (p_r) of pipe P_i . The mass flow is denoted accordingly, so that the interconnection dictates the simplified algebraic constraints,

$$\tilde{p}_{1,r} = \tilde{p}_{2,r} = \tilde{p}_{0,\ell}, \quad (13a)$$

$$\tilde{q}_{0,\ell} = \tilde{q}_{1,r} + \tilde{q}_{2,r}. \quad (13b)$$

The first equation is related to continuity and the second represents conservation of mass at the junction. This composite joint model would have a state of dimension six:

$\begin{bmatrix} \tilde{p}_{0,r} & \tilde{p}_{1,r} & \tilde{p}_{2,r} & \tilde{q}_{0,\ell} & \tilde{q}_{1,\ell} & \tilde{q}_{2,\ell} \end{bmatrix}^\top$, in lexicographic ordering, plus the algebraic constraints, (13). However, due to (13a) we can omit $\tilde{p}_{2,r}$ as a state (which would naturally arise in three pipe models (9)).

Define α_1 and α_2 to be the parameters in (9) for pipes 1 and 2, and

$$\delta = \frac{\alpha_1}{\alpha_1 + \alpha_2}. \quad (14)$$

Then, the six-state composite joint system plus constraint (13) may be rewritten as an unconstrained five-state system

$$\begin{aligned} \dot{x}_t &= A_j x_t + B_j u_t, \\ y_t &= C_j x_t + D_j u_t, \end{aligned}$$

with

$$A_j = \begin{bmatrix} 0 & 0 & -\alpha_0 & 0 & 0 \\ 0 & 0 & \alpha_1(1-\delta) & -\alpha_1(1-\delta) & -\alpha_1(1-\delta) \\ \beta_0 & \kappa_0 & \gamma_0 & 0 & 0 \\ 0 & \beta_1 & 0 & \gamma_1 & 0 \\ 0 & \beta_2 & 0 & 0 & \gamma_2 \end{bmatrix}, \quad (15a)$$

$$B_j = \begin{bmatrix} 0 & 0 & \alpha_0 \\ 0 & 0 & 0 \\ 0 & 0 & 0 \\ \kappa_1 & 0 & 0 \\ 0 & \kappa_2 & 0 \end{bmatrix}, C_j = \begin{bmatrix} 1 & 0 & 0 & 0 & 0 \\ 0 & 0 & 0 & 1 & 0 \\ 0 & 0 & 0 & 0 & 1 \end{bmatrix}, \quad (15b)$$

$$D_j = 0_{3 \times 3}. \quad (15c)$$

The state, input and output vectors are now

$$\begin{aligned} x_t &= \begin{bmatrix} \tilde{p}_{0,r} & \tilde{p}_{1,r} & \tilde{q}_{0,\ell} & \tilde{q}_{1,\ell} & \tilde{q}_{2,\ell} \end{bmatrix}^\top, \\ u_t &= \begin{bmatrix} \tilde{p}_{1,\ell} & \tilde{p}_{2,\ell} & \tilde{q}_{0,r} \end{bmatrix}^\top, \\ y_t &= \begin{bmatrix} \tilde{p}_{0,r} & \tilde{q}_{1,\ell} & \tilde{q}_{2,\ell} \end{bmatrix}^\top. \end{aligned}$$

Calculation of the steady-state gain from input three, $q_{0,r}$, to outputs two, $q_{1,\ell}$, and three, $q_{2,\ell}$, shows that, in steady state,

$$\begin{aligned} \tilde{q}_{1,\ell} + \tilde{q}_{2,\ell} &= \frac{\beta_1 \gamma_2}{\beta_1 \gamma_2 + \beta_2 \gamma_1} \tilde{q}_{0,r} + \frac{\beta_2 \gamma_1}{\beta_1 \gamma_2 + \beta_2 \gamma_1} \tilde{q}_{0,r}, \\ &= \tilde{q}_{0,r}. \end{aligned}$$

That is, this five-state composite joint model satisfies the conservation of mass flow, (13b). Constraint (13a) is redundant, since the variables $\tilde{p}_{2,r}$ and $\tilde{p}_{0,\ell}$ have been removed;

they can be computed from (13a). The new model parameter δ , defined in (14), describes the nominal proportion of flow $\tilde{q}_{0,\ell}$ attributed to each of the feeding pipes. This is the formal process of removing the constraint from the DAE of index 1.

7.2 Branch

Differently from the joint, for the branch in Figure 8(b) the equality constraint on the pressures relates the state variable, $p_{0,r}$, to input signals of the single pipe model of the branching pipes, $\tilde{p}_{1,\ell}$ and $\tilde{p}_{2,\ell}$, i.e.,

$$\tilde{p}_{0,r} = \tilde{p}_{1,\ell} = \tilde{p}_{2,\ell}, \quad (16a)$$

$$\tilde{q}_{0,r} = \tilde{q}_{1,\ell} + \tilde{q}_{2,\ell}, \quad (16b)$$

so that the dimension of the composite model does not reduce, but is equal to the direct sum of those of the single pipe models of the individual pipes. Similarly, constraint (16b) on the mass flows does not prescribe any interdependence of any input variables, but rather sets the input signal of the single pipe model of pipe P_0 as the sum of two other state variables. Hence, an additional parameter, such as δ for the joint is absent. The related matrices for a branch model are

$$A_b = \begin{bmatrix} 0 & 0 & 0 & -\alpha_0 & \alpha_0 & \alpha_0 \\ 0 & 0 & 0 & 0 & -\alpha_1 & 0 \\ 0 & 0 & 0 & 0 & 0 & -\alpha_2 \\ \beta_0 & 0 & 0 & \gamma_0 & 0 & 0 \\ \kappa_1 & \beta_1 & 0 & 0 & \gamma_1 & 0 \\ \kappa_2 & 0 & \beta_2 & 0 & 0 & \gamma_2 \end{bmatrix}, \quad (17a)$$

$$B_b = \begin{bmatrix} 0 & 0 & 0 \\ 0 & \alpha_1 & 0 \\ 0 & 0 & \alpha_2 \\ \kappa_0 & 0 & 0 \\ 0 & 0 & 0 \\ 0 & 0 & 0 \end{bmatrix}, C_b = \begin{bmatrix} 0 & 1 & 0 & 0 & 0 & 0 \\ 0 & 0 & 1 & 0 & 0 & 0 \\ 0 & 0 & 0 & 1 & 0 & 0 \end{bmatrix}, \quad (17b)$$

with state $x_t = \begin{bmatrix} \tilde{p}_{0,r} & \tilde{p}_{1,r} & \tilde{p}_{2,r} & \tilde{q}_{0,\ell} & \tilde{q}_{1,\ell} & \tilde{q}_{2,\ell} \end{bmatrix}^\top$, input $u_t = \begin{bmatrix} \tilde{p}_{0,\ell} & \tilde{q}_{1,r} & \tilde{q}_{2,r} \end{bmatrix}^\top$ and output $y_t = \begin{bmatrix} \tilde{p}_{1,r} & \tilde{p}_{2,r} & \tilde{q}_{0,\ell} \end{bmatrix}^\top$. The feedthrough matrix D_b is zero.

Remark 3 It is straightforward to expand these ideas to intersections comprising m -input pipes and n -output pipes. This construction is available at [5] and generalizes the systematic reduction of index-1 DAEs to systems of ODEs.

7.3 Pipes in series

N pipes in series are depicted in Figure 9, and are of particular interest if pipe parameters (see Table 1) change along the dimension of x or the discretization error grows too large for a given length. For conciseness we only state the rele-

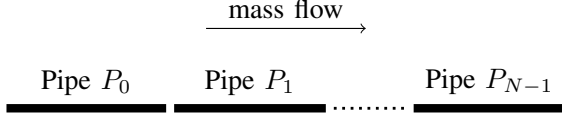


Fig. 9. Pipe series

vant matrices here that result from the continuity conditions and conservation of mass, i.e.,

$$\tilde{p}_{i,r} = \tilde{p}_{i+1,\ell}, \quad \tilde{q}_{i,r} = \tilde{q}_{i+1,\ell}, \quad (18)$$

with $i \in \{0, 1, \dots, N-2\}$. The state, input and output elements $p_{i,r}$ and $q_{i,\ell}$ in lexicographical order, i.e., $x_t = [\tilde{p}_{0,r} \dots \tilde{p}_{N-1,r} \quad \tilde{q}_{0,\ell} \dots \tilde{q}_{N-1,\ell}]^\top$, $u_t = [\tilde{p}_{0,\ell} \quad \tilde{q}_{N-1,r}]^\top$ and $y_t = [\tilde{p}_{N-1,r} \quad \tilde{q}_{0,\ell}]^\top$, yield

$$A_s = \begin{bmatrix} \mathbf{0} & A_{s,12} \\ A_{s,21} & A_{s,22} \end{bmatrix}, B_s = \begin{bmatrix} B_{s,1}^\top & B_{s,2}^\top \end{bmatrix}^\top, \\ C_s = \begin{bmatrix} \mathbf{0}_{2,2(N-1)} & I_2 & \mathbf{0}_{2,2(N-1)} \end{bmatrix},$$

and $D_s = \mathbf{0}$, where the subscripts for $\mathbf{0}$ and I describe the dimension and

$$A_{s,12} = \begin{bmatrix} -\alpha_0 & \alpha_0 & & \mathbf{0} \\ & \ddots & \ddots & \\ & & \ddots & \alpha_{N-2} \\ \mathbf{0} & & & -\alpha_{N-1} \end{bmatrix}, \\ A_{s,21} = \begin{bmatrix} \beta_0 & & \mathbf{0} \\ \kappa_1 & \ddots & \\ & \ddots & \ddots \\ \mathbf{0} & \kappa_{N-1} & \beta_{N-1} \end{bmatrix}, \\ A_{s,22} = \text{diag}(\gamma_0, \gamma_1, \dots, \gamma_{N-1}), \\ B_{s,1} = \begin{bmatrix} \mathbf{0}_{2(N-1),2} \\ 0 \quad \alpha_{N-1} \end{bmatrix}, B_{s,2} = \begin{bmatrix} \kappa_0 & 0 \\ \mathbf{0}_{2(N-1),2} \end{bmatrix}.$$

Since each pipe conforms to steady-state conservation of mass flow, the interconnection automatically does as well. Bode diagrams are provided in [5] for 2i2o models of a 30-meter pipe section as: a single 30m pipe, two 15m pipes in series, three 10m pipes in series; low-frequency responses coincide.

8 Systematic Model Interconnection

Building on the composite models above, we introduce a matrix formulation that enables the construction of state-space models for interconnected components of pipes, joints and branches.

8.1 Matrix methodology

Towards this goal, with N interconnected components, let $\mathcal{U}_i \subset \mathbb{R}^{n_{u,i}}$ and $\mathcal{Y}_i \subset \mathbb{R}^{n_{y,i}}$ be the set of inputs and outputs for component i , respectively, with state $x_t^{(i)} \in \mathbb{R}^{n_{x,i}}$, input $u_t^{(i)} \in \mathbb{R}^{n_{u,i}}$ and output $y_t^{(i)} \in \mathbb{R}^{n_{y,i}}$. The model matrices are denoted accordingly. Further, $\bar{\mathcal{U}}$ and $\bar{\mathcal{Y}}$ are the respective sets of external inputs and outputs. We assume that the input of every component is either connected to the output of another component or represents an external input.

Assumption 1 (connectedness) Let $i \in \{1, 2, \dots, N\}$. For any $u \in \mathcal{U}_i$ there exists a $j \in \{1, 2, \dots, N\}, j \neq i$, such that $u \in \mathcal{Y}_j \cup \bar{\mathcal{U}}$.

Internal interconnections are governed by the continuity of pressure and mass flow per (18). We begin by stacking the state-space models of the individual network components. With some abuse of notation,

$$\dot{\bar{x}}_t = A\bar{x}_t + B\bar{w}_t, \quad \bar{y}_t = C\bar{x}_t + D\bar{w}_t \quad (19)$$

where

$$A = \text{blkdiag}(A^{(1)}, A^{(2)}, \dots, A^{(N)}), \quad (20a)$$

$$B = \text{blkdiag}(B^{(1)}, B^{(2)}, \dots, B^{(N)}), \quad (20b)$$

$$C = \text{blkdiag}(C^{(1)}, C^{(2)}, \dots, C^{(N)}), \quad (20c)$$

$$D = \text{blkdiag}(D^{(1)}, D^{(2)}, \dots, D^{(N)}). \quad (20d)$$

The total state vector, $\bar{x}_t \in \mathbb{R}^{n_{x,1}+n_{x,2}+\dots+n_{x,N}}$, total output vector, $\bar{y}_t \in \mathbb{R}^{n_{y,1}+n_{y,2}+\dots+n_{y,N}}$, and *component* input vector, $\bar{w}_t \in \mathbb{R}^{n_{u,1}+n_{u,2}+\dots+n_{u,N}}$ are composed correspondingly of direct sums. Assumption 1 yields

$$\bar{w}_t = F\bar{y}_t + G\bar{u}_t, \quad (21)$$

where \bar{u}_t denotes the total input vector of external signals feeding into the total system. The matrix F describes connections between component inputs and outputs, and G is related to the connection between external inputs and internal components. Hence, both matrices are sparse and constructed as follows,

$$[F]_{i,j} = \begin{cases} 1, & \text{if } [\bar{y}_t]_j = [\bar{w}_t]_i, \\ 0, & \text{otherwise,} \end{cases} \quad (22a)$$

$$[G]_{i,j} = \begin{cases} 1, & \text{if } [\bar{u}_t]_j = [\bar{w}_t]_i, \\ 0, & \text{otherwise,} \end{cases} \quad (22b)$$

with $[\cdot]_{i,j}$ denoting the matrix element in row i and column j , and vectors written accordingly. This formulation is applied to a numerical example in Section 9. It allows us to define a state model of the total system.

Proposition 4 *A (perhaps non-minimal) state-space realization of (19) and (21) is given by*

$$\bar{x}_t = \bar{A}\bar{x}_t + \bar{B}\bar{u}_t, \quad \bar{y}_t = \bar{C}\bar{x}_t + \bar{D}\bar{u}_t, \quad (23)$$

where

$$\begin{aligned} \bar{A} &= A + BF(I - DF)^{-1}C, & \bar{C} &= (I - DF)^{-1}C, \\ \bar{B} &= B[I + F(I - DF)^{-1}D]G, & \bar{D} &= (I - DF)^{-1}DG. \end{aligned}$$

PROOF. Substituting \bar{w} from (21) into (19) for \bar{y}_t yields

$$\begin{aligned} \bar{y} &= (I - DF)^{-1}C\bar{x}_t + (I - DF)^{-1}DG\bar{u}_t, \\ \bar{w} &= F(I - DF)^{-1}C\bar{x}_t + [I + F(I - DF)^{-1}D]G\bar{u}_t. \end{aligned} \quad (24)$$

Now substituting from (24) into (19) for $\dot{\bar{x}}_t$ produces the closed-loop state-space connected system.

$$\begin{aligned} \dot{\bar{x}}_t &= [A + BF(I - DF)^{-1}C]\bar{x}_t \\ &\quad + B[I + F(I - DF)^{-1}D]G\bar{u}_t, \\ \bar{y}_t &= (I - DF)^{-1}C\bar{x}_t + (I - DF)^{-1}DG\bar{u}_t. \end{aligned}$$

Here, the total output, \bar{y}_t , is set to be the outputs of all components. However, if only some variables constitute to the total output modifying \bar{y}_t is a simple exercise through the multiplication of \bar{C} and \bar{D} by an appropriate selection matrix.

8.2 Subsuming Mason

Next, we show that the state-space realization above subsumes Mason's Gain Formula [18]. The latter is a method to find transfer functions of SFGs with multiple inputs and multiple outputs and has also been established in a simple matrix form in e.g. [8]. The interest in this equivalence result lies in its generality for linear systems and advantage over Mason's Gain Formula via simple matrix manipulation without relying on symbolic matrix inversions with transfer functions as matrix elements. Further, the calculation in Proposition 4 yields all the closed-loop transfer functions between each input and each output, versus Mason, which computes SISO transfer functions using Cramer's Rule.

Mason's Gain Formula formulation in [8] starts by writing the vector of output signals, \bar{y} , as the interconnection of $y_t^{(i)}$ and \bar{u}_t with transfer function matrices,

$$\bar{y}_t = \mathcal{Q}\bar{y}_t + \mathcal{P}\bar{u}_t. \quad (25)$$

Mason's Gain Formula is then that the solution is given by

$$\bar{y}_t = (I - \mathcal{Q})^{-1}\mathcal{P}\bar{u}_t. \quad (26)$$

Proposition 5 *A state-variable realization of Mason's Gain Formula transfer function, $(I - \mathcal{Q})^{-1}\mathcal{P}$, is given in (23).*

This is proven in the Appendix.

9 Numerical experiment

We apply our modeling methodology to the loop illustrated in Figure 10, which represents a hypothetical pipe loop at the GCTF. Such a feedback system creates problems for DAE methods, such as those in [3], because of the algebraic constraints. Here we use it as a proof-of-concept test case and rely, rather unrealistically but similarly to [3] for distribution networks, on isothermal models and treatment of the compressor and valve as static gains. Clearly, the thermal properties of compressors, heat exchangers and valves play an important role on the spatial scales of gas processing facilities and these will form the focus for ongoing modeling.

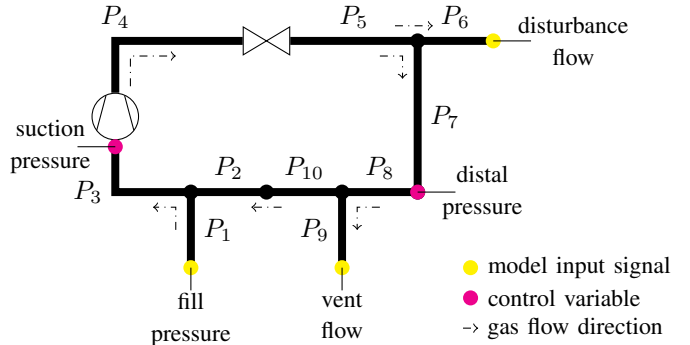


Fig. 10. Pipe network with compressor and valve \bowtie . In process control parlance, the fill pressure and vent flow are manipulated variables, the suction and distal pressures are controlled variables, and the flow from P_6 is a disturbance signal.

The gas is methane and flows clockwise, entering through pipe P_1 and exiting through pipes P_6 and P_9 . The aim is to regulate the pressures $p_{3,r}$ and $p_{7,r}$ in the face of leakage via P_6 . The Haaland formula [22] and assumed parameters⁴ yield a friction factor for each pipe of $\lambda = 0.0111$.

9.1 Network model

The compressor and valve, whose corresponding variables are respectively labeled by subscripts c and v , are modeled

⁴ All pipes are assumed to have the same geometry, i.e., $L = 10\text{m}$, $d = 0.7\text{m}$, roughness $= 4.57 \times 10^{-5}\text{m}$. Further, we assume that $Re \approx 1.168 \times 10^8$, $T_0 = 300\text{K}$, $z_0 = 0.95$, $R_s = 518.28\text{J}/(\text{Kmol})$, $\tilde{p}_{ss,\ell} = 25 \times 10^5\text{Pa}$ and $\tilde{q}_{ss} = 21\text{m}^2/\text{s}^2$.

as static gains

$$D_c = \begin{bmatrix} k_c & 0 \\ 0 & 1 \end{bmatrix}, \quad D_v = \begin{bmatrix} k_v & 0 \\ 0 & 1 \end{bmatrix},$$

where $k_c = 4$ and $k_v = 0.8$. Further, pipes (P_1, P_2, P_3) are modeled as a joint, as in (15), and (P_5, P_6, P_7) and (P_8, P_9, P_{10}) as branches, as in (17). Composing the system according to (20), results in the component input vector,

$$\bar{w}_t = \begin{bmatrix} \tilde{p}_{1,\ell} & \tilde{p}_{2,\ell} & \tilde{q}_{3,r} & \tilde{p}_{c,\ell} & \tilde{q}_{c,r} & \tilde{p}_{4,\ell} & \tilde{q}_{4,r} & \tilde{p}_{v,\ell} & \tilde{q}_{v,r} & \tilde{p}_{5,\ell} & \tilde{q}_{6,r} & \tilde{q}_{7,r} & \tilde{p}_{8,\ell} & \tilde{q}_{9,r} & \tilde{q}_{10,r} \end{bmatrix}^\top,$$

and the total output vector,

$$\bar{y}_t = \begin{bmatrix} \tilde{p}_{3,r} & \tilde{q}_{1,\ell} & \tilde{q}_{2,\ell} & \tilde{p}_{c,r} & \tilde{q}_{c,\ell} & \tilde{p}_{4,r} & \tilde{q}_{4,\ell} & \tilde{p}_{v,r} & \tilde{q}_{v,\ell} & \tilde{p}_{6,r} & \tilde{p}_{7,r} & \tilde{q}_{5,\ell} & \tilde{p}_{9,r} & \tilde{p}_{10,r} & \tilde{q}_{8,\ell} \end{bmatrix}^\top.$$

The inputs of the total system are

$$\bar{u}_t = \begin{bmatrix} \tilde{p}_{1,\ell} & \tilde{q}_{6,r} & \tilde{q}_{9,r} \end{bmatrix}^\top.$$

With (22), the total input and output vector, \bar{u}_t and \bar{y}_t , as well as the component input vector, \bar{w}_t , are the basis for the construction of F and G . For example, $[\bar{w}_t]_1 = \tilde{p}_{1,\ell}$ is an input of the total system and the first element of \bar{u}_t . Hence $[G]_{1,1} = 1$. Further, $[\bar{w}_t]_2 = \tilde{p}_{2,\ell}$ connects to $\tilde{p}_{10,r} = [\bar{y}_t]_{14}$, so that $[F]_{2,14} = 1$. Similarly, $[\bar{w}_t]_{11} = \tilde{q}_{6,r}$ is another total input, i.e., $\tilde{q}_{6,r} = [\bar{u}_t]_2$, so that $[G]_{11,2} = 1$. In this way, by passing through \bar{w}_t and following (22), we can fill the matrices with ones at the appropriate location and zeros otherwise. The eigenvalues of the resulting interconnected system all have negative real part; hence stability is demonstrated. Some eigenvalues have large imaginary parts pointing to the high-oscillatory resonant modes, which we ignore in the control design, which will recognize the presence of anti-aliasing filters in the sensors [7].

9.2 Steady state: conservation of mass

The isothermal LTI closed-loop system is stable with the overall pressure static gains from $\tilde{p}_{1,\ell}$ to all but $\tilde{p}_{2,r}$ greater than one. Increasing the compressor and/or valve gains can bring about instability, as might be expected. Further, since the frequency response of each component is available, standard stability tests may be performed. Indeed, the control design is to construct a stabilizing 2-input/2-output regulator to reject the effect of the disturbance flow.

To evaluate the model in terms of conservation of mass, we also analyze the steady-state gains from the three loop

inputs, $\tilde{p}_{1,\ell}$, $\tilde{q}_{6,r}$ and $\tilde{q}_{9,r}$, to each pipe's mass flow. The corresponding DC-gain values are shown in Table 2. Each column represents one model input and each row shows the corresponding steady-state change in mass flow from nominal due to a unit step change of the respective input and zero inputs otherwise.

to\from	fill: $\tilde{p}_{1,\ell}$	vent: $\tilde{q}_{9,r}$	dist: $\tilde{q}_{6,r}$
$\tilde{q}_{1,\ell}$	0	1	1
$\tilde{q}_{2,\ell}$	0.184	-1.022	-0.8
$\tilde{q}_{3,\ell}$	0.184	-0.022	0.2
$\tilde{q}_{4,\ell}$	0.184	-0.022	0.2
$\tilde{q}_{5,\ell}$	0.184	-0.022	0.2
$\tilde{q}_{6,\ell}$	0	0	1
$\tilde{q}_{7,\ell}$	0.184	-0.022	-0.8
$\tilde{q}_{8,\ell}$	0.184	-0.022	-0.8
$\tilde{q}_{9,\ell}$	0	1	0
$\tilde{q}_{10,\ell}$	0.184	-1.022	-0.8

Table 2

DC (steady-state) gains from inputs to mass flows.

9.2.1 Step response fill pressure change

Evaluating the first column with input $\tilde{p}_{1,\ell}$, a zero change in mass flows $\tilde{q}_{6,\ell}, \tilde{q}_{9,\ell}$ is consistent the other zero inputs, $\tilde{q}_{9,r} = \tilde{q}_{6,r} = 0$. As a result, the steady-state mass flow $\tilde{q}_{1,\ell} = 0$. A higher fill pressure leads to a larger mass flow around the loop, uniformly through all pipes, as evident by the numerical values of the other rows of the same column.

9.2.2 Step responses vent and disturbance flow changes

Evaluating the second column with input $\tilde{q}_{9,r} = 1$ and zero disturbance flow, i.e. $\tilde{q}_{6,r} = 0$ (and hence $\tilde{q}_{6,\ell} = 0$), 1 kg/s^2 enters the loop through $\tilde{q}_{9,r}$ so that $\tilde{q}_{9,\ell} = 1$. We further note that mass flow around the loop uniformly dropped by -0.022 excluding pipes P_{10} and P_2 . The flow through Pipe P_{10} and P_2 reduces by -1.022 as a result of the reduced overall flow and unit flow exiting through pipe P_9 . Then, the additional flow $\tilde{q}_{1,\ell} = 1$ through pipe P_1 brings the flow back to -0.022 . The same reasoning can be applied to the last column related to the disturbance input $\tilde{q}_{6,r}$.

Our analysis shows that conservation of mass around the loop is captured through the use of composite models and the matrix methodology presented above, without imposing additional algebraic constraints. Further, the linear time-invariant model is amenable to direct feedback controller design and stability analysis.

10 Conclusion and further directions

In this paper, we present control-oriented models in the form of LTI state-space realizations that capture the dominant dy-

namics for the pressure, mass flow and temperature in pipes at a scale appropriate for gas processing facilities. Validation against real-world data and simulation of the initial constituent equations illustrate their suitability for model-based controller design, which will incorporate requirements for robustness to minor static offsets and slow variations. Building on these models, we elaborate on the need for composite elements for interconnections to absorb DAEs, and provide a corresponding catalog of composite models for common units. To increase practical relevance of the proposed model, we also introduce a matrix methodology that enables a simple creation of pipe networks and illustrate its behavior with a numerical experiment. The analysis of costs and benefits of nonisothermal models indicates and quantifies inaccuracies of the models and distinguishes between models parametrized by nominal temperature versus those parametrized by measured temperatures. Here, we focus on process control; additional (nonlinear) control systems across multiple operating points may be employed for safety, start-up and shutdown and these could be local to specific units, and rapid in their action. Our methods are not targeted towards these controllers.

The control-oriented modeling developed here draws guidance at the formulation stage from the control objective specification in the introduction. Two companion works take these methods further. In [6], the modeling methods are applied to a generate linear state-space models for a wider variety of network elements. This paper provides a compendium of modeled elements together with their derivation and proof of internal satisfaction of conservation rules. The compendium also provides example MATLAB code illustrating the connection process for models. Thus, [6] is a support document. The technical partner paper [7] on the other hand marries the control-oriented modeling with model-based control and provides strong evidence of the role played by model features here in subsequent controller development. Particularly, [7] explores in detail the regulation control effect of the mass-conserving models.

Acknowledgement

This research was supported by funding from Solar Turbines Incorporated, who also provided operating data and guidance.

References

- [1] R. Alamian, M. Behbahani-Nejad, and A. Ghanbarzadeh. A state space model for transient flow simulation in natural gas pipelines. *Journal of Natural Gas Science and Engineering*, 9:51 – 59, 2012.
- [2] M. Behbahani-Nejad and A. Bagheri. A MATLAB Simulink Library for Transient Flow Simulation of Gas Networks. *World Academy of Science, Engineering and Technology, International Journal of Mechanical, Aerospace, Industrial, Mechatronic and Manufacturing Engineering*, 2:873–879, 2008.
- [3] P. Benner, S. Grundel, C. Himpe, C. Huck, T. Streubel, and C. Tischendorf. Gas Network Benchmark Models. In S. Campbell, A. Ilchmann, V. Mehrmann, and T. Reis, editors, *Applications of Differential-Algebraic Equations: Examples and Benchmarks. Differential-Algebraic Equations Forum*. Springer, Cham., 2018.
- [4] W. Borutsky. *Bond Graph Methodology: Development and Analysis of Multidisciplinary Dynamic System Models*. Springer London, 2010.
- [5] Sven Brüggemann and Robert R. Bitmead. Control-Oriented Modeling of Pipe Flow through Intersecting Pipe Geometries. *arXiv preprint: 2112.06974*, 2021.
- [6] Sven Brüggemann, Robert H. Moroto, and Robert R. Bitmead. A Compendium of Control-Oriented Models of Gas Processing Equipment Components. *arXiv preprint: 2211.06813*, 2022.
- [7] Sven Brüggemann, Robert H. Moroto, and Robert R. Bitmead. Control-orientation, conservation of mass and model-based control of compressible fluid networks. *IEEE Transactions on Control System Technology*, submitted:(arXiv preprint: 2211.06826), 2022.
- [8] Huaichen Chen. The matrix expression of signal flow graph and its application in system analysis software. *Chinese Journal of Electronics*, 11(3):361–364, 2002.
- [9] Hector Delgado-Garibay, Nathan Poerner, Donghui Zhang, Rainer Kurz, and Greg Phillippi. Chapter 12 - compressor testing. In Klaus Brun and Rainer Kurz, editors, *Compression Machinery for Oil and Gas*, pages 449–461. Gulf Professional Publishing, 2019.
- [10] Rolf Findeisen and Frank Allgöwer. Nonlinear model predictive control for index-one dae systems. In F. Allgöwer and A. Zheng, editors, *Nonlinear Model Predictive Control. Progress in Systems and Control Theory*, volume 26, pages 145–161. Birkhäuser, Basel, 2000.
- [11] P. Garabedian. *Partial Differential Equations*. AMS Chelsea Publishing Series. Chelsea Publishing Company, 1986.
- [12] Anurag Goyal, Marcel A. Staedter, and Srinivas Garimella. A review of control methodologies for vapor compression and absorption heat pumps. *International Journal of Refrigeration*, 97:1–20, 2019.
- [13] S. E. Haaland. Simple and Explicit Formulas for the Friction Factor in Turbulent Pipe Flow. *Journal of Fluids Engineering*, 105(1):89–90, 03 1983.
- [14] J.P. Holman. *Heat Transfer*. McGraw-Hill Education, 2009.
- [15] Christoph Huck and Caren Tischendorf. Topology motivated discretization of hyperbolic PDAEs describing flow networks. Technical report, Humboldt-Universität zu Berlin, 2017.
- [16] J. Králík, P. Stiegler, Z. Vostrý, and J. Závorka. *Dynamic modeling of large-scale networks with application to gas distribution*. Elsevier, 1988.
- [17] Michael V. Lurie. *Modeling of Oil Product and Gas Pipeline Transportation*. John Wiley & Sons, Ltd, 2008.
- [18] S. J. Mason. Feedback theory-further properties of signal flow graphs. *Proceedings of the IRE*, 44(7):920–926, 1956.
- [19] Andrzej J. Osiadacz and Maciej Chaczykowski. Comparison of isothermal and non-isothermal pipeline gas flow models. *Chemical Engineering Journal*, 81(1):41–51, 2001.
- [20] Venugopal Pichai, Mesut E. Sezer, and Dragoslav D. Šiljak. A Graph-Theoretic Algorithm for Hierarchical Decomposition of Dynamic Systems with Applications to Estimation and Control. *IEEE Transactions on Systems, Man, and Cybernetics*, SMC-13(2):197–207, 1983.
- [21] Bryan P Rasmussen and Andrew G Alleyne. Control-Oriented Modeling of Transcritical Vapor Compression Systems. *Journal of Dynamic Systems, Measurement, and Control*, 126(1):54–64, Apr 2004.
- [22] D.C. Rennels and H.M. Hudson. *Pipe Flow: A Practical and Comprehensive Guide*. Wiley, 2012.

- [23] Ascher H. Shapiro. *The Dynamics and Thermodynamics of Compressible Fluid Flow*, volume I. John Wiley & Sons, 1953.
- [24] Dragoslav D. Šiljak. Stability of large-scale systems. *IFAC Proceedings Volumes*, 5(1, Part 4):75–85, 1972. IFAC 5th World Congress: Part 4, Paris, France, June 12-17, 1972.
- [25] Dragoslav D. Šiljak. *Large-Scale Dynamic Systems*. Dover Publications, 1978.
- [26] Matthew A. Williams, Justin P. Koeln, Herschel C. Pangborn, and Andrew G. Alleyne. Dynamical Graph Models of Aircraft Electrical, Thermal, and Turbomachinery Components. *Journal of Dynamic Systems, Measurement, and Control*, 140(4), 12 2017. 041013.

A Proofs

Proposition 1

By hypothesis and with $q = \rho A_c v$, equation (3b) results directly from the Momentum and Gas Equations, (1b) and (1d), see e.g. [3].

For the pressure-related PDE, let $a_1 \doteq \frac{c_v}{R_s z_0} - \frac{R_s z_0}{2A_c^2} \frac{q^2 T}{p^2} + \frac{gh}{R_s T z_0}$. Then, solving energy equation (1c) for $\frac{\partial p}{\partial t}$ yields

$$\frac{\partial p}{\partial t} = a_1^{-1} \left(q\rho + \frac{\partial T}{\partial t} \underbrace{\left(\frac{ghp}{R_s T^2 z_0} - \frac{R_s z_0 q^2}{2A_c^2 p} \right)}_{\doteq -a_2} - \frac{R_s z_0 T q}{A_c^2 p} \frac{\partial q}{\partial t} - \frac{\partial}{\partial x} \left[\frac{q}{A_c} (c_v T + gh) + \frac{q^3 R_s^2 T^2 z_0^2}{2p^2 A_c^3} + \frac{q R_s T z_0}{A_c} \right] \right).$$

From Continuity and Gas Equations, resp. (1a) and (1d),

$$\frac{\partial T}{\partial t} = \frac{z_0 R_s T^2}{p A_c} \frac{\partial q}{\partial x} + \frac{T}{p} \dot{p}, \quad (\text{A.1})$$

since $(a_1 + \frac{T}{p} a_2)^{-1} = \frac{R_s z_0}{c_v}$ and, using (3b), yields

$$\begin{aligned} \frac{\partial p}{\partial t} = & \frac{R_s z_0}{c_v} \left(q\rho + \frac{\partial q}{\partial x} \left(\frac{gh}{A_c} + \frac{3R_s^2 z_0^2 q^2}{2A_c^3 p^2} \right) + \frac{R_s z_0 T q}{A_c^2 p} \left[A_c \frac{\partial p}{\partial x} \right. \right. \\ & + A_c \left(\frac{z_0 R_s q^2}{A_c^2 p} \frac{\partial T}{\partial x} - \frac{z_0 R_s T q^2}{A_c^2 p^2} \frac{\partial p}{\partial x} \right) + \frac{\lambda z_0 R_s T}{2DA_c p} q|q| \\ & \left. \left. + gA_c \frac{p}{z_0 R_s T} \frac{dh}{dx} \right] \right. \\ & \left. - \frac{\partial}{\partial x} \left[\frac{q}{A_c} (c_v T + gh) + \frac{q^3 R_s^2 T^2 z_0^2}{2p^2 A_c^3} + \frac{q R_s T z_0}{A_c} \right] \right). \end{aligned}$$

Computing the spatial derivative leads to

$$\begin{aligned} \frac{\partial p}{\partial t} = & \frac{R_s z_0}{c_v A_c} \left[q\rho A_c - \frac{\partial q}{\partial x} T (c_v + R_s z_0) + \frac{\partial p}{\partial x} \frac{R_s z_0 T q}{p} \right. \\ & \left. - \frac{\partial T}{\partial x} q (c_v + R_s z_0) + \frac{\lambda R_s^2 z_0^2 T^2 q^2 |q|}{2DA_c^2 p^2} \right], \end{aligned}$$

which with (2) results in (3a).

For the temperature, we use the result above and (A.1) to obtain

$$\begin{aligned} \frac{\partial T}{\partial t} = & \frac{R_s z_0 T}{c_v A_c p} \left[q\rho A_c - \frac{\partial q}{\partial x} T R_s z_0 + \frac{\partial p}{\partial x} \frac{R_s z_0 T q}{p} \right. \\ & \left. - \frac{\partial T}{\partial x} q (c_v + R_s z_0) + \frac{\lambda R_s^2 z_0^2 T^2 q^2 |q|}{2DA_c^2 p^2} \right], \end{aligned}$$

which with (2) results in (3c).

Proposition 5

For readability we exclude the subscript t in this proof. From (19), state-variable realizations of the transfer functions \mathcal{Q} and \mathcal{P} are given by the following:

$$\mathcal{Q} = [D + C(sI - A)^{-1}B]F, \quad (\text{A.2})$$

$$\mathcal{P} = [D + C(sI - A)^{-1}B]G. \quad (\text{A.3})$$

Firstly, use the matrix inversion formula to write

$$\begin{aligned} (I - \mathcal{Q})^{-1} = & \{I - [D + C(sI - A)^{-1}B]F\}^{-1}, \\ = & (I - DF)^{-1} + \\ & (I - DF)^{-1}C[sI - A - BF(I - DF)^{-1}C]^{-1} \\ & BF(I - DF)^{-1}. \end{aligned} \quad (\text{A.4})$$

Define the \bar{u} -component of \bar{w} as $\bar{w}^{\bar{u}} = [I + F(I - DF)^{-1}D]G\bar{u} = w_1^{\bar{u}} + Fw_2^{\bar{u}}$ with $w_1^{\bar{u}} = G\bar{u}$ and $w_2^{\bar{u}} = (I - DF)^{-1}DG\bar{u}$ and appeal to linearity to define

$$\begin{aligned} \dot{\bar{x}}_1 = & [A + BF(I - DF)^{-1}C]\bar{x}_1 + B\bar{w}_1^{\bar{u}}, \\ \dot{\bar{x}}_2 = & [A + BF(I - DF)^{-1}C]\bar{x}_2 + BF\bar{w}_2^{\bar{u}}, \\ \bar{y} = & (I - DF)^{-1}C(\bar{x}_1 + \bar{x}_2) + \bar{w}_2^{\bar{u}}. \end{aligned}$$

From here and the definitions of $w_1^{\bar{u}}$ and $w_2^{\bar{u}}$, it is apparent that $\bar{y} = \bar{y}_1 + \bar{y}_2$ where,

$$\dot{\bar{x}}_1 = [A + BF(I - DF)^{-1}C]\bar{x}_1 + BG\bar{u}, \quad (\text{A.5})$$

$$\bar{y}_1 = (I - DF)^{-1}C\bar{x}_1, \quad (\text{A.6})$$

and

$$\dot{\bar{x}}_2 = [A + BF(I - DF)^{-1}C]\bar{x}_2 + BF(I - DF)^{-1}DG\bar{u}, \quad (\text{A.7})$$

$$\bar{y}_2 = (I - DF)^{-1}C\bar{x}_2 + (I - DF)^{-1}DG\bar{u}, \quad (\text{A.8})$$

System 1 (A.5)-(A.6): Denote the system transfer function $\mathcal{K} = (I - DF)^{-1}C(sI - A)^{-1}B$ and rewrite (A.5) as output feedback around \mathcal{K} .

$$\dot{\bar{x}}_1 = A\bar{x}_1 + B(F\bar{y}_1 + G\bar{u}).$$

In turn, writing this in terms of \mathcal{K} and using (A.4) for $(I - \mathcal{Q})^{-1}$, we have

$$\begin{aligned} \bar{y}_1 &= \mathcal{K}(F\bar{y}_1 + G\bar{u}) \\ &= (I - \mathcal{K}F)^{-1}\mathcal{K}G\bar{u} \\ &= [I - (I - DF)^{-1}C(sI - A)^{-1}BF]^{-1} \\ &\quad (I - DF)^{-1}C(sI - A)^{-1}BG\bar{u} \\ &= \{I + (I - DF)^{-1}C[sI - A - BF(I - DF)^{-1}C]^{-1} \\ &\quad BF\}(I - DF)^{-1}C(sI - A)^{-1}BG\bar{u} \\ &= \{(I - DF)^{-1} + (I - DF)^{-1}C[sI - A - BF \\ &\quad (I - DF)^{-1}C]^{-1}BF(I - DF)^{-1}\}C(sI - A)^{-1}BG\bar{u}, \\ &= (I - \mathcal{Q})^{-1}C(sI - A)^{-1}BG\bar{u}. \end{aligned} \quad (\text{A.9})$$

System 2 (A.7)-(A.8): Directly comparing (A.4) to (A.7)-(A.8), we see that

$$\bar{y}_2 = (I - \mathcal{Q})^{-1}DG\bar{u}. \quad (\text{A.10})$$

Combining (A.9) and (A.10) we have

$$\begin{aligned} \bar{y} &= \bar{y}_1 + \bar{y}_2, \\ &= (I - \mathcal{Q})^{-1}C(sI - A)^{-1}BG\bar{u} + (I - \mathcal{Q})^{-1}DG\bar{u}, \\ &= (I - \mathcal{Q})^{-1}\mathcal{P}\bar{u}. \end{aligned}$$

■